On the Simulation of Thermal Isomerization of Molecular Photoswitches in Biological Systems

Amirhossein Bakhtiiari, Gustavo J. Costa, and Ruibin Liang*

ACCESS | Metrics & More | Article Recommendations | Supporting Information

ABSTRACT: Molecular photoswitches offer precise, reversible photocontrol over biomolecular functions and are promising light-regulated drug candidates with minimal side effects. Quantifying thermal isomerization rates of photoswitches in their target biomolecules is essential for fine-tuning their light-controlled drug activity. However, the effects of protein binding on isomerization kinetics remain poorly understood, and simulations are crucial for filling this gap. Challenges in the simulation include describing multireference electronic structures near transition states, disentangling competing reaction pathways, and sampling protein−ligand interactions. To overcome these challenges, we

used multiscale simulations to characterize the thermal isomerization of photostatins (PSTs), which are light-regulated microtubule inhibitors for potential cancer phototherapy. We employed a new ab initio multireference electronic structure method in a quantum mechanics/molecular mechanics setting and combined it with enhanced sampling techniques to characterize the *cis* to *trans* free-energy profiles of three PSTs in a vacuum, aqueous solution, and tubulin dimer. The significant advantage of our novel approach is the efficient treatment of the multireference character in PSTs' electronic wavefunction throughout the conformational sampling of protein−ligand interactions along their isomerization pathways. We also benchmarked our calculations using high-level ab initio multireference electronic structure methods and explored the competing isomerization pathways. Notably, calculations in a vacuum and implicit solvent models cannot predict the order of the PSTs' thermal half-lives in the aqueous solution observed in the experiment. Only by explicitly treating the solvent molecules can the correct order of isomerization kinetics be reproduced. Protein binding perturbs free-energy barriers due to hydrogen bonding between PSTs and nearby polar residues. Our work generates comprehensive, high-quality benchmark data and offers guidance for selecting computational methods to study the thermal isomerization of photoswitches. Ab initio multireference free-energy calculations in explicit molecular environments are crucial for predicting the effects of substituents on the thermal half-lives of photoswitches in biological systems.
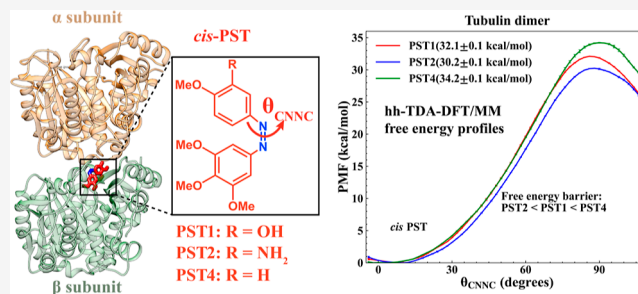
INTRODUCTION

Photoisomerization of molecular photoswitches results in conformational changes that can be leveraged to control biomolecular structures and functions with high spatial and temporal resolution using light.[1−4] This class of photoswitches can be designed and synthesized by incorporating photoactive functional groups into molecules interacting with target biomolecules. For example, enzyme inhibitors and signaling lipids can be turned into photoswitches by adding an azobenzene (AB) moiety to their chemical structure. In the active state of the photoswitch, it mimics the original molecule's protein−ligand interactions and triggers similar protein activity. In the inactive state, these interactions with the target protein are reduced or altered, resulting in different protein activities. This contrast between the two isomers makes photoswitches valuable tools for understanding the biochemical and biophysical processes at the molecular level. They also allow precise and reversible manipulation of biochemical and biophysical processes through photocontrol, paving the way for light-regulated therapeutics with fewer side

effects than traditional options. Isomerization of photoswitches can also occur through thermal fluctuations near room temperature. Unlike photoisomerization which involves transitions between electronically excited and ground states, thermal isomerization typically only involves the ground state.

Quantifying the thermal isomerization kinetics of photoswitches in biomolecular environments is crucial for designing light-regulated drugs. If the active isomer is less stable than the inactive one, the drug's activity will decay over time as the active isomer undergoes thermal isomerization. This can happen if the photoswitches move outside the illuminated area or if the illumination is turned off. It is often desirable for
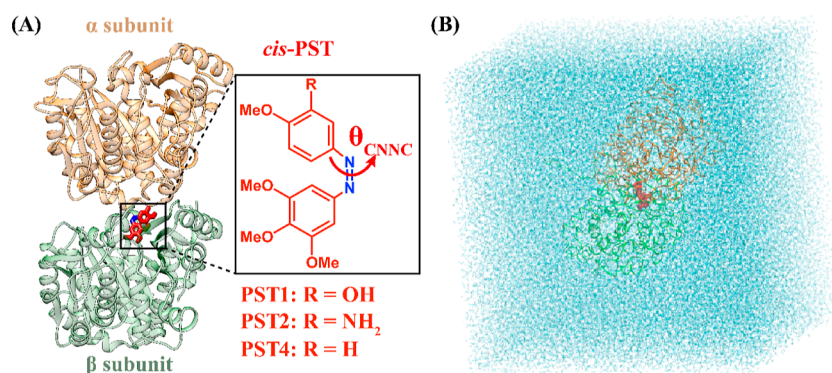
Figure 1. (A) *cis*-PST binds to the interface of the α and β subunits of tubulin, which disrupts the polymerization of the tubulin monomers. Rotation around the central torsion θ_{CNNC} by either thermal relaxation or photoisomerization leads to *trans*-PST, which unbinds from the protein and terminates the inhibition. The three derivatives of PSTs differ in the R group (labeled in the text) and their *cis* isomers' thermal lifetimes. (B) System setup of a tubulin dimer (orange and green) bound with *cis*-PST solvated in a periodic box of water molecules (blue).

photoswitches to quickly deactivate themselves once they leave the illuminated area, minimizing the side effects on healthy cells. In applications with repeated on-and-off illumination cycles, such as the photopharmacological treatment of degenerative retinal diseases,[4] it is important to fine-tune thermal half-lives to match the frequency of the illumination cycle.

Investigating the effects of protein binding on the thermal isomerization kinetics in biomolecules is challenging experimentally, making molecular simulations essential for understanding the design principles. However, accurately predicting the thermal isomerization kinetics of molecular photoswitches in biomolecular environments is computationally difficult for three reasons. First, for AB- or stilbene-based photoswitches, isomerization involves rotation around a double bond (N=N or C=C). The transition state usually has a near-perpendicular torsion around the bond, causing ground- and first-excited-state energies to come close together. Electronic wavefunctions exhibit multireference characters in such transition states, with significant contributions from both closed-shell and open-shell singlet electron configurations. Popular single-reference methods like density functional theory (DFT), although computationally inexpensive and commonly used,[5−8] cannot accurately describe transition-state structures and isomerization pathways.[9]

Second, the isomerization of AB-based molecular photoswitches occurs through competing pathways involving intersystem crossing, bending angle inversion, or hydrazone tautomer. Ground-state isomerization from *cis*-to-*trans* isomer may involve two intersystem crossing events (S_0 to T_1, followed by T_1 to S_0), which could lower the energy barrier compared to pathways involving only the S_0 state.[9,10] Bending the C−N=N angle to nearly 180° is an alternative mechanism to the central torsion rotation. The hydrazone tautomer mechanism suggests that the transient protonation of the N=N bond lowers the bond order and hence the isomerization barrier. This is possible when benzyl ring substituents increase the pK_a's of N atoms, making the overall energy barrier kinetically favorable in protic solutions. Calculations that explicitly treat protonation/deprotonation reactions on photoswitches are necessary to evaluate the likelihood of this mechanism.

Finally, it is computationally challenging to sample conformational fluctuations of the protein−ligand interactions during thermal isomerization, which gives rise to non-

negligible enthalpic and entropic contributions to the free-energy barriers. A previous study employed force field-based free-energy calculations to reveal that interactions between combretastatin A-4 (CA-4) and tubulin dimer change the ligand's isomerization barriers.[11] However, this study lacked the accuracy of first-principles electronic structure calculations and cannot model the electron density response to the protein environment during isomerization. Additionally, specific protein−ligand interactions like hydrogen bonds are difficult to model with implicit solvents. To our knowledge, few studies have employed ab initio multireference methods for characterizing the thermal isomerization free-energy barriers of photoswitches in explicit solvents or biomolecules.

To fill these gaps, in this study, we used multiscale simulations to comprehensively investigate the ground-state isomerization mechanism of photostatins (PSTs),[12] a class of AB-based photoswitches designed for the reversible control of microtubule (MT) polymerization dynamics. MTs play crucial roles in cell proliferation,[13] and inhibitors that disrupt MT dynamics are effective anticancer chemotherapeutics.[14] However, traditional MT inhibitors can cause severe side effects due to their nonspecific cytotoxicity.[15,16] PSTs, as photoswitchable analogues of the chemotherapeutics CA-4, enable reversible inhibition of MT through illumination. Under ∼400 nm light, *cis*-PSTs bind to tubulin subunits, inhibiting polymerization and inducing cell death. In dark conditions or under ∼510 nm light, *trans*-PST detaches from tubulin, restoring mitosis.[12] The PSTs thus allow precise light control over tumor cell mitosis and death.[12]

We employed enhanced sampling simulations and the hole−hole Tamm−Dancoff-Approximated DFT (hh-TDA-DFT)[17,18] in a quantum mechanics/molecular mechanics (QM/MM) setting to characterize the isomerization free-energy profiles of three PSTs (Figure 1A) in three different environments. The hh-TDA-DFT method can effectively treat multireference electronic structures and has a similar cost to time-dependent DFT (TD-DFT). It has been widely tested and proven reliable for examining the photodynamics of AB- and stilbene-derived photoswitches in a vacuum,[19] explicit solution,[20] and biomolecular systems.[21−23] Our results quantify the *cis* → *trans* isomerization free-energy barriers for the PSTs in a vacuum, aqueous solution, and tubulin. Moreover, we performed extensive benchmark calculations using the extended multistate complete active space second-order perturbation theory (XMS-CASPT2)[24−27] to validate the hh-

TDA-DFT method and explore alternative pathways. Our findings revealed the significance of explicitly treating the molecular environment in accurately predicting experimental free-energy barriers. Protein environments influence barriers through hydrogen-bonding interactions with PSTs. We also analyzed and compared isomerization mechanisms involving singlet−triplet intersystem crossing, bending angle inversion, and hydrazone tautomer, highlighting the importance of using multireference methods and explicit solvation in the calculations.

METHODS

System Setup. A dimer consisting of one α and one β subunit of tubulin was extracted from chain C and chain D of the crystal structure (PDB code 5LYJ[11]). This structure features a *cis* CA-4 molecule bound in the interface between the two monomers. The Modeller software package[28] was used to add the missing residues from the PDB structure. The H++ online server[29] was used to add hydrogen atoms and assign protonation states of all ionizable residues at a pH value of 6.5. The initial geometry of PST1 was obtained by converting the two carbon atoms in the C=C double bond of *cis* CA-4 to two nitrogen atoms. The PST2 and PST4 geometries were generated by replacing the R group on PST1. Crystal waters were discarded since they are all on the surface of the protein and can be easily accessed by water molecules in bulk solution. The system was solvated in a box of water molecules and charge-neutralized with Na^+ ions using the tleap plugin in the Amber20 software package.[30] The abovementioned setup resulted in a periodic boundary condition (PBC) simulation box with an initial size of $122.1 \times 144.8 \times 145.8$ Å^3.

Most of the force field parameters of the PSTs were parameterized following the general AMBER force field procedure.[31,32] The parameters for the central C−N=N−C torsion (θ_{CNNC} in Figure 1) and the two nearby C−C−N=N torsions were fitted to reproduce the PES along these coordinates obtained at the hh-TDA-BHHLYP/6-31G* level of theory. The parameters for the protein-bound GTP were obtained from the previous study.[33] The protein and water molecules were modeled with Amberff14SB[34,35] and SPF/Fw force fields,[36] respectively. The justifications of using the crystal structure of CA-4 to build PSTs in the tubulin are elaborated in the "Computational Method" section of the Supporting Information and Figure S1.

In addition to the protein system setup, we also set up the *cis*-PSTs solvated in a box of SPC/Fw water molecules, resulting in a PBC simulation box with an initial size of $62.9 \times 62.3 \times 65.8$ Å^3.

Classical MD Equilibration. Each of the PST-bound tubulin systems was first minimized for 2000 steps and equilibrated in the constant *NVT* ensemble at 300 K temperature for 10 ps. Harmonic positional restraints with force constants of 10 kcal/mol/Å^2 were placed on the heavy atoms of the protein and PST. Then, the system was further equilibrated in the constant NPT ensemble at 300 K temperature and 1 atm pressure for 5 ns, where the harmonic restraints gradually vanished. Following this, production run in the same constant *NPT* ensemble was continued for 50 ns. The timestep of the simulation was 1 fs. In both *NVT* and *NPT* simulations, a Langevin thermostat was used to maintain the temperature with a collision frequency of 1 ps^{-1}. In constant *NPT* simulations, the pressure was controlled by a Berendsen barostat with a pressure relaxation time of 2 ps. The van der

Waals interactions cutoff was 10 Å, and the particle-mesh Ewald method was used for calculating the electrostatic interactions.

To prepare the initial structures of QM/MM umbrella sampling (US) along the central θ_{CNNC} torsion, US simulations using MM force field were first performed to restrain this collective variable at different values. In particular, the last snapshot of the unbiased classical MD simulation with *cis*-PSTs was selected, and 21 umbrella windows were evenly spaced to cover a range of 0−100° for the window centers. In each window, a harmonic potential with a force constant of 200 kcal/mol/radian^2 was applied to restrain the torsion close to the window center. The biased simulation was performed for 5 ns in each window to relax the system in response to the twisting of the PST. The classical MD simulation for PSTs in an aqueous solution followed the abovementioned procedure.

Ab Initio Multireference QM/MM US Simulations. The US simulations were performed for each PST in a vacuum, aqueous solution, and tubulin to quantify the free-energy barrier of *cis* → *trans* thermal isomerization on the S_0 state. For the simulations in aqueous solution and tubulin, the QM/MM US simulations were performed with the same force constants and window centers as the MM US simulations described above. The initial structure for each QM/MM US window was prepared from the last snapshot of the MM US window with the same window center with open boundary conditions. The tubulin dimer, GTP, Mg^{2+} ions, PST, and all other molecules with any atom within 10 Å of the PST were selected from the MM snapshot. For the aqueous solution simulation setup, the cutoff used for atom selection was the same, except for the absence of protein. The QM region included only the PST, which was treated with hh-TDA-BHHLYP/6-31G*. The MM region included the rest of the system, which was treated with the same force field as that for the classical MD equilibration. Electrostatic embedding was used to treat the electrostatic interactions between QM and MM atoms. The QM/MM umbrella simulation was performed for all windows for at least 6 ps at 300 K temperature, and some windows had longer simulations for convergence. The first 1 ps simulation was discarded as equilibration, and the rest was used for calculating the potential of mean forces (PMFs) by the weighted histogram analysis method algorithm.[37,38] Statistic uncertainties in the PMFs were performed by block average analysis. For QM/MM US simulations in a vacuum, the initial geometry for each window was obtained from constrained geometry optimization with hh-TDA-BHHLYP/6-31G*. Combining the simulations for all PSTs in all environments, the total amount of enhanced sampling at the hh-TDA-BHHLYP level of theory (with a similar cost to TD-DFT) was at least 945 ps. To the best of our knowledge, the extensive amount of enhanced sampling at this level of ab initio accuracy (see "Results") in explicit molecular environments was unprecedented for molecular photoswitches.

Benchmark PES Calculations of Neutral PSTs in a Vacuum. The calculations of PESs of neutral PSTs in a vacuum were performed using both XMS-CASPT2 and hh-TDA-BHHLYP methods to benchmark the accuracy of hh-TDA-BHHLYP for predicting the following properties: (1) energy barriers along the S_0 isomerization pathway; (2) energy barriers along the $S_0 \rightarrow T_1 \rightarrow S_0$ pathway which involves two intersystem crossings; (3) relative energy barriers between the rotation and inversion mechanisms. To this end, the calculations included: (1) constrained geometry optimization

along the central θ_{CNNC} torsion for both the S_0 and T_1 states; (2) constrained geometry optimization along one of the C—N=N bending angles (α_{CNN}) on the S_0 state; (3) spin—orbit coupling (SOC) calculations at the highest crossing point of S_0 and T_1 states using the restricted active space state interaction (RASSI) level of theory.[39] It is worth noting that all XMS-CASPT2 PESs correspond to the geometries optimized using XMS-CASPT2 gradients. For all XMS-CASPT2 calculations, the reference wavefunction was obtained from state-average CASSCF calculations with an active space of 10 electrons and 8 orbitals and three lowest singlet states, with cc-pVDZ basis set (XMS-CASPT2/SA-3-CASSCF(10e,8o)/cc-pVDZ). The active space utilized for constructing the SA-3-CASSCF wavefunction consists of one lone-pair orbitals (n) localized at the nitrogen atoms along with seven π orbitals. Figure S2 in the Supporting Information displays the orbitals of this active space. The three lowest singlet states were used in the XMS-CASPT2 calculations, and an imaginary shift of 0.2 a.u. was applied. The IPEA (ionization potential-electron affinity) shift correction was not applied. For constrained optimizations on the T_1 state, single-state CASPT2 (SS-CASPT2) was employed using the reference wavefunction from the single-state CASSCF(10e, 8o)/cc-pVDZ calculations of the lowest triplet state. Core orbitals were frozen in all CASPT2 calculations. As a result, both static and dynamic correlation effects on the electronic energies were considered by the perturbatively modified electronic CASSCF wavefunctions of the singlet and triplet states. All constrained optimizations using hh-TDA-BHHLYP were done with the 6-31G* basis set.

The reaction rates through the S_0 isomerization pathway in a vacuum were estimated using the transition-state theory via Eyring's equation

$$k_{TST} = \frac{k_B T}{h} \cdot e^{-\beta \Delta E} \qquad (1)$$

where ΔE is the free-energy barrier, β equals $1/(k_B T)$, k_B is Boltzmann's constant, T is the temperature (298.0 K), and h is the Planck constant. The free-energy barriers were approximated by the potential energy barriers.

The minimum energy crossing point (MECPs) structures of the PST systems between the S_0 and T_1 states were approximated as the highest point in the lower trace of the S_0 and T_1 PESs obtained using constrained geometry optimizations (Figure 7C,D). The Computational Methods section of the Supporting Information provides a more detailed description of our approach and a discussion of its justification (Figures S5 and S6 and Tables S1–S3). Using these approximate MECP geometries, the SOC matrix elements (H_{SO}) between the S_0 and T_1 states were calculated at the XMS-CASPT2/SA($S = 3, T = 1$)-CASSCF(10e, 8o)/cc-pVDZ level of theory, employing the atomic mean-field integral[40] approach in combination with the spin—orbit RASSI approach. The effective SOCs are calculated by eq 2

$$H_{SO,eff} = \sqrt{H_{SO_1}^2 + H_{SO_0}^2 + H_{SO_{-1}}^2} \qquad (2)$$

where -1, 0, and 1 indicate the T_1 state's three components.

The nonadiabatic transition-state theory (NA-TST)[9,41,42] was employed to describe the reaction rate (k_{NA-TST}) and quantify the timescale (t_{NA-TST}) of the events at ISC geometry for the PST family in the gas phase using eq 3

$$k_{NA-TST} = k_{ISC} \cdot e^{-\beta \Delta E} \qquad (3)$$

where ΔE is the energy difference between the cis-PST minima on the S_0 state and the highest crossing point between the S_0 and T_1 states. k_{ISC} is the intersystem crossing rate calculated using eq 4[9,41,42]

$$k_{ISC} = \frac{\pi^{3/2} \alpha}{2h \sqrt{\lambda/(k_B T)}} \cdot \left[1 + \frac{1}{2} \cdot \exp\left(\frac{1}{12\alpha^2 (k_B T \lambda)^3} \right) \right] \qquad (4)$$

The α and λ values in eq 4 can be computed from eqs 5 and 6

$$\alpha = \frac{4H_{SO}^{3/2}}{\hbar} \cdot \left(\frac{\mu}{F_g |\Delta \mathbf{F}|} \right)^{1/2} \qquad (5)$$

$$\lambda = \frac{|\Delta \mathbf{F}|}{2F_g H_{SO}} \qquad (6)$$

where $\Delta F, F_g$ and μ are defined in eqs 7–9

$$\Delta \mathbf{F} = \mathbf{F}_{T_1} - \mathbf{F}_{S_0} \qquad (7)$$

$$F_g = \left| \sum_{j=1}^{N} \sum_{n=1}^{3} (\mathbf{F}_{S_0})_{jn} (\mathbf{F}_{T_1})_{jn} \right|^{1/2} \qquad (8)$$

$$\mu = \left(\frac{1}{|\Delta \mathbf{F}|^2} \sum_{j=1}^{N} \sum_{n=1}^{3} \Delta \mathbf{F}_{jn}^2 m_n^{-1} \right)^{-1} \qquad (9)$$

F_g is the geometric mean of the forces of the S_0 and T_1 electronic states at the crossing point. $\Delta \mathbf{F}$ represents the difference between the forces of the S_0 and T_1 electronic states at the crossing point. They were calculated at the same XMS-CASPT2 level of theory as described above. μ is the reduced mass of the system, m_n's are the atomic masses of each atom of the molecule, and $\hbar$ is the reduced Planck constant.

Characterization of PES in Implicit Solvents. Relaxed PES scans were performed in both the vacuum and conductor-like polarizable continuum model (C-PCM)[43,44] for aqueous solution (with a 78.39 dielectric constant). The constrained optimizations were performed on both the S_0 and T_1 states for all three PSTs using the spin-flip time-dependent DFT (SF-TD-DFT)[45] with the 6-31G* basis set and the BHHLYP functional.

Characterization of Isomerization Mechanism through the Hydrazone Tautomer Intermediate of Protonated PST. To explore the feasibility of ground-state isomerization through the hydrazone tautomer of protonated PST, a thermodynamic cycle (Figure 2) was first constructed to estimate the pKa's of the N atoms in the N=N double bond of PSTs.

DFT optimizations of protonated and deprotonated cis-PSTs were performed using B3LYP/6-311**G++ in a vacuum and C-PCM with a dielectric constant of 78.39. In the protonated PST, one of the two N atoms was protonated. The optimized structures were used to calculate the pKa's of PSTs using eq 10[46]

$$\Delta G_{ion}(sol) = G(A_{gas}^-) + G(H_{gas}^+) - G(AH_{gas}) + \Delta G_{sol}(A^-)$$
$$+ \Delta G_{sol}(H^+) - \Delta G_{sol}(AH) \qquad (10)$$

where $\Delta G_{ion}(sol)$ is the ionization free energy in solution and is associated with the pKa value of the PST, and $G(A_{gas}^-)$,
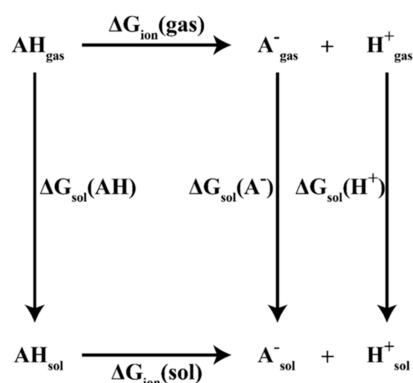
Figure 2. Thermodynamic cycle for calculating the pKa's of the central N atoms.

$G(H_{gas}^+)$, and $G(AH_{gas})$ are the absolute free energies in the gas phase for the conjugate base, the proton, and the conjugate acid, respectively. $G(H_{gas}^+) = -6.28$ kcal/mol $+ RT\ln(24.46) = -4.39$ kcal/mol in the gas-phase 1 M standard state at 298 K temperature.[47] $G(A_{gas}^-)$ and $G(AH_{gas})$ were approximated by their potential energies at the *cis* minima optimized by B3LYP/6-311++G**. $\Delta G_{sol}(A^-)$, $\Delta G_{sol}(H^+)$, and $\Delta G_{sol}(AH)$ are the solvation free energies of the three species. $\Delta G_{sol}(H^+) = -265.9$ kcal/mol in the gas-phase 1 M standard state.[47] $\Delta G_{sol}(A^-)$ and $\Delta G_{sol}(AH)$ were calculated using the C-PCM with B3LYP/6-311++G**.

The pK_a's of PSTs were further calibrated based on the calculated and experimental pK_a's of *trans*-AB. To this end, pK_a of *trans*-AZB was calculated using the same method. The difference between the calculated pK_a's of *trans*-AZB and *cis*-PSTs was added to the experimental pK_a of *trans*-AZB to estimate the absolute pK_a's of the *cis*-PSTs. Our test calculations suggested that the pK_a's of both N atoms in PST1 are within 0.05, so the pK_a's for only one of them was calculated in all PSTs.

The free-energy cost for the protonation of PST at pH 7, leading to the hydrazone tautomer was calculated by eq 11

$$\Delta G_{protonation} = \ln(10)RT(7.0 - pK_a) \tag{11}$$

The isomerization barrier of the hydrazone tautomer along the C−NH⁺−N−C torsion was calculated by constrained optimization using the hh-TDA-BHHLYP/6-31G* method. The total energetic barrier for the hydrazone pathway was estimated by adding the free-energy change of protonating PSTs at pH = 7 (Eq 11) and the isomerization barrier in the hydrazone tautomer.

All XMS-CASPT2-constrained optimizations were performed using BAGEL[48,49] interfaced with a modified version of the "geomeTRIC" software packages.[50] All SOC calculations were performed with the OpenMolcas package.[51] All constrained optimizations using hh-TDA-BHHLYP and QM/MM simulations were performed with the TERACHEM software package. All SF-TD-DFT calculations were performed with the ORCA software package.[52] All classical MD simulations were performed with Amber20 software package.[30] All US simulations were performed with the PLUMED plugin.[53−55]

■ RESULTS

Effect of Environment on the *cis* → *trans* Isomerization of Free-Energy Barriers. To understand how the environment affects the thermal isomerization kinetics of PSTs,

we performed extensive QM/MM US simulations of the *cis* → *trans* isomerization process of three PSTs in a vacuum, water, and tubulin dimer (Figure 3), where the hh-TDA-BHHLYP
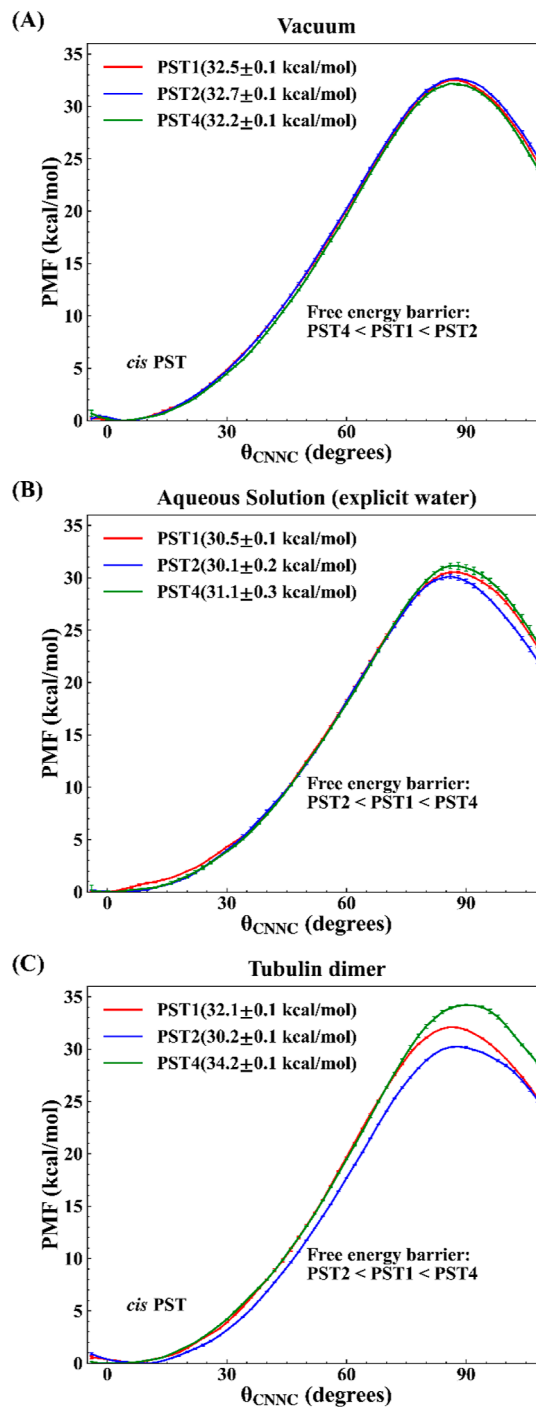
Figure 3. Ab initio ground-state PMFs for the *cis* → *trans* isomerization of PST1, PST2, and PST4 along the central torsion θ_{CNNC} in a vacuum, explicit aqueous solution, and tubulin dimer. The QM method is hh-TDA-BHHLYP for all PMFs. The order of free-energy barriers in the aqueous solution is consistent with the order or thermal half-lifetimes of the PSTs measured by the experiments in similar conditions[12] (Table 1). However, the order of free-energy barriers in a vacuum is the opposite of that in an aqueous solution. The protein environment in tubulin enlarges the differences in the free-energy barriers of PSTs.

method was selected as the QM method. The accuracy of this method is extensively benchmarked in the following sections. The simulation results showed that the free-energy barrier for the isomerization of PSTs is affected by the environment. In an aqueous solution, the free-energy barriers (Figure 3B) match the experimental order of thermal half-lives of *cis*-PSTs (Table 1).

Table 1. Experimental Half-Lives (τ) of *cis*-PSTs Measured in Aqueous Solution at pH = 7.4 (Adapted from Ref 12)

	τ (min)
PST1	6.2
PST2	0.8
PST4	83.0

However, in a vacuum, the order of free-energy barriers (Figure 3A) is opposite to the experimental trend in the aqueous environment. The barriers are decreased by 1−2.6 kcal/mol when moving from a vacuum to the aqueous solution, and the magnitude of the change in barriers is different for each PST. This suggests that solvation has a non-negligible effect on both the absolute values and relative order of isomerization barriers. Moreover, the effect of the protein environment on the isomerization barrier varies depending on the PST (Figure 3C). For instance, the tubulin dimer environment significantly increases the barrier of PST4 by 3 kcal/mol but only slightly increases the barriers of PST1 and PST2 by 0.6 and 0.1 kcal/mol, respectively (Figure 3C).

To further understand the effects of the aqueous environment on the transition state's stability, we calculated the radial distribution functions (RDFs) between the PST and the water molecules, which are averaged over the QM/MM US trajectories around the *cis* minima and TSs for each PST. The RDFs are shown in Figure S7. Specifically, two types of RDFs are calculated. The first type is between all water molecules' oxygen atoms (O(WAT)) and the two nitrogen atoms in the N═N bond (N1 and N2). The second type is between all water oxygen atoms (O(WAT)) and the hydroxyl oxygen (O2), the amine nitrogen (N3), and the hydrogen (H18) in the R substituent group of PST1, PST2, and PST4 (defined in Figure 1). The umbrella windows used for calculating the RDFs in the *cis* minima are centered at 0, 5, and 10° of θ_{CNNC}, respectively. The umbrella windows used for calculating the RDFs in the TSs are centered at 80, 85, and 90°, respectively.

It is evident from Figure S7 that the solvation structures around the PSTs are different between the *cis* minima and the TSs for all three PSTs. For example, for the RDFs between N1,N2 and O(WAT) (Figure S7A,C,E), the first peak near 2.8 Å is consistently lower in the *cis* minima than the TSs, while the second minimum near 4 Å is consistently higher in the *cis* minima than the TSs. For the RDFs between the heavy atom in the R group and water oxygen atoms (Figure S7B,D), the first minimum near 3.5 Å is consistently lower in the *cis* minima than the TSs. For PST4, the R group is a single hydrogen atom (H18), and the RDF between it and water oxygen atoms has a much lower first peak in the *cis* minimum than the TS.

We also compared the stability of water-mediated intramolecular hydrogen bonds between the *cis* minima and TSs. Specifically, for PST1 and PST2, we calculated the frequencies of observing a continuous chain of water-mediated hydrogen

bonds connecting the heavy atom of the R group to the N1 atom of the N═N bond, with the criterion that the chain has at most five hydrogen bonds (Table S4). It is evident that transitioning from the *cis* minimum to the TS largely increases the stability of the water-mediated intramolecular hydrogen bond. Also, the water-mediated intramolecular hydrogen bonds are more stable in PST2 than PST1. Given the abovementioned differences between the minima and the TS in the solvation structure and hydrogen-bonding environment, we conclude that the explicit solvent is necessary to correctly predict the relative order of isomerization kinetics among the PSTs in aqueous solution.

As described above, the free-energy barriers of the three PSTs change differently upon switching to the protein environment. This phenomenon results from the distinct hydrogen-bonding patterns between the PSTs and the protein environment (Figures 4 and 5). Specifically, *cis*-PST1 forms hydrogen bonds with ASN258 and LYS352 in chain D (Figure 4A); near the transition state (Figure 5A), the hydrogen bond with ASN258 switches to VAL181 in chain C. *cis*-PST2 is hydrogen-bonded with ASN258 in chain D and THR179 in chain C (Figure 4B); near the transition state (Figure 5B), the bond with ASN258 changes to ALA180 in chain C. *cis*-PST4 is hydrogen-bonded with ASP251 and ASN258 in chain D (Figure 4C) but only with ASP251 near the transition state (Figure 5C). These findings suggest that protein binding affects the thermal isomerization kinetics of the three PSTs differently because of different protein−ligand interactions.

In contrast to MD simulations using MM force fields, in QM/MM calculations, it remains challenging to decompose the total energy of the system into interaction energies arising from the hydrogen-bond, steric, and electrostatic interactions. To further understand the contributions of steric and electrostatic effects at the QM/MM level, in principle, it is possible to computationally mutate the residues lining the PSTs' binding pocket to change the protein−PST interactions. However, it requires setting up new hh-TDA-DFT/MM US simulations, which are computationally too expensive. We reason that the steric interactions between different PSTs and the protein environment are similar due to the similar structure of the PSTs. Their only difference is in the R group substituent on one of the benzyl rings, which can result in different hydrogen-bond interactions with the surrounding molecules. Thus, our analysis is focused on the hydrogen bonds between the PSTs and their environment, such as the water molecules and the polar residues in the binding site.
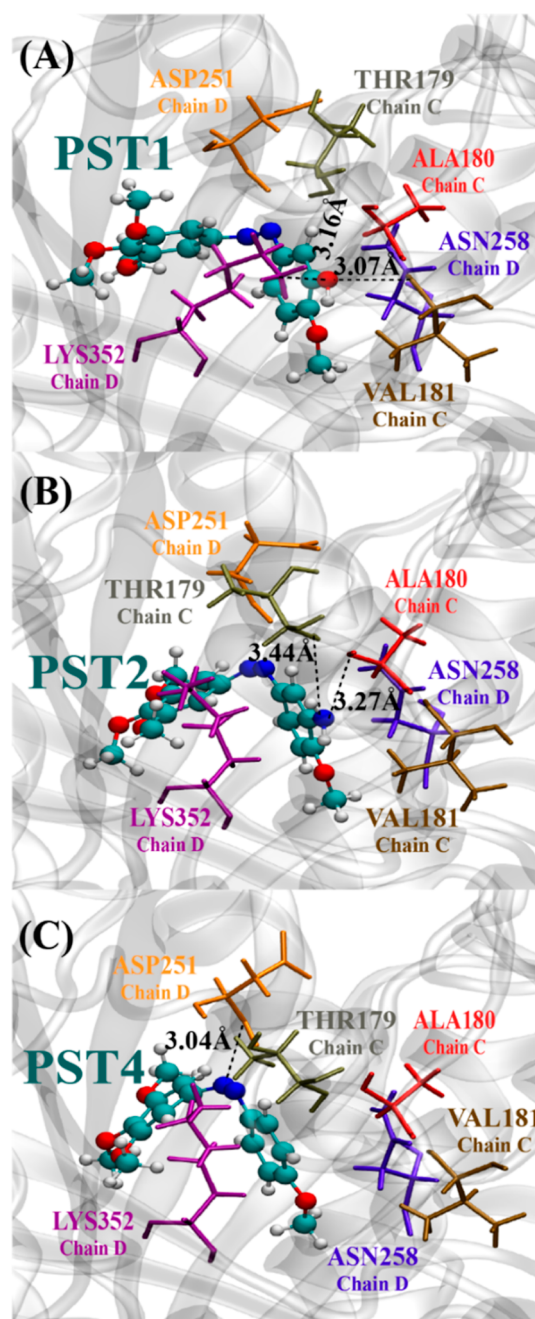
Benchmark Calculations of Hh-TDA-DFT Using XMS-CASPT2. Previous computational studies have proposed three thermal isomerization pathways for molecular photoswitches derived from AB, with a focus on the prototypical AB molecule. These pathways include (1) torsion of central θ_{CNNC} on the S_0 state, (2) rotation of central θ_{CNNC} involving $S_0 \rightarrow T_0 \rightarrow S_0$ intersystem crossing, and (3) inversion of one of the α_{CNN} angles. Among these mechanisms, the inversion-assisted torsion mechanism, which combines (2) and (3), is widely accepted in this field. Here, we conducted a comparison between the hh-TDA-BHHLYP and XMS-CASPT2 methods for predicting the barriers of the three PSTs along each of the three pathways. Our extensive benchmark calculations support the use of hh-TDA-BHHLYP calculations for free-energy calculations on the S_0 state, as described above. Furthermore, these calculations contribute to resolving the ongoing debate
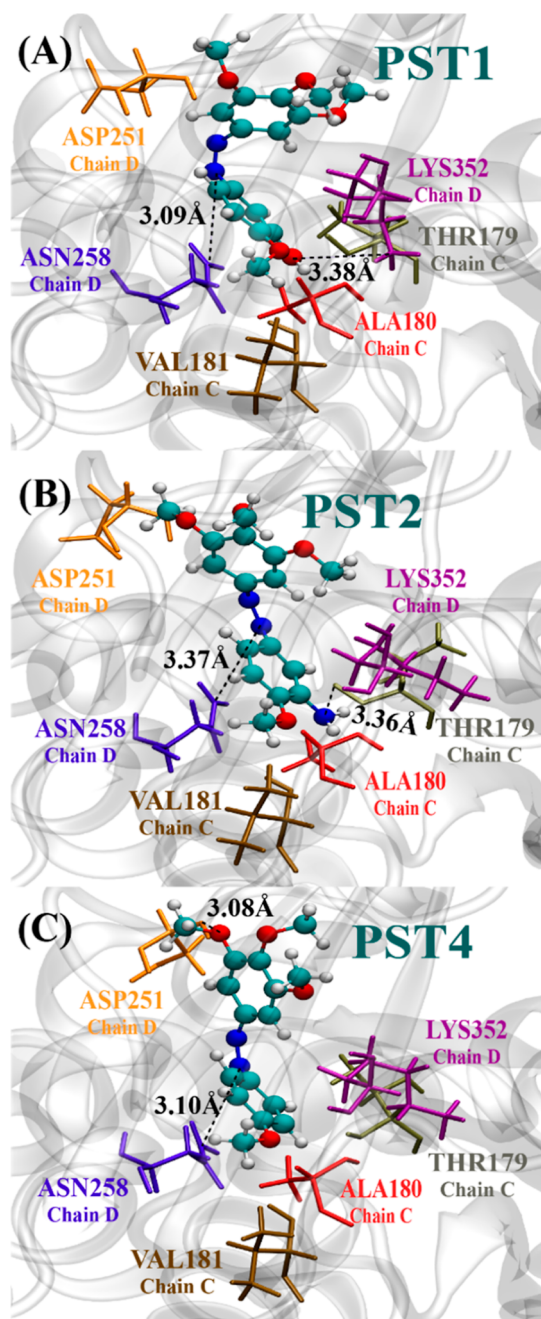
Figure 4. Intermolecular hydrogen-bond interactions between PSTs and tubulin residues at the dihedral near 10° (*cis* minima). Distances of hydrogen bonds are labeled near the dashed black lines. The PSTs are rendered as balls and sticks, and the surrounding residues as colored sticks with their chain IDs in the original crystal structure (Chain C: α subunit; Chain D: β subunit).


Figure 5. Intermolecular hydrogen-bond interactions between PSTs and tubulin residues at the dihedral near 80° (close to the transition state). Distances of hydrogen bonds are labeled near the dashed black lines. The PSTs are rendered as balls and sticks, and the surrounding residues as colored sticks with their chain IDs in the original crystal structure (Chain C: α subunit; Chain D: β subunit).

regarding the competing isomerization pathways of AB-derived photoswitches.

Pathway 1: Isomerization through Torsion on S_0 State. The PES along θ_{CNNC} on the S_0 state was determined through constrained optimization using the XMS-CASPT2 and hh-TDA-BHHLYP methods (Figure 6). Both methods indicate that the energy barriers for the *cis* → *trans* isomerization of the three PSTs are within 1 kcal/mol of each other. The order of barrier heights predicted by both methods is PST4 < PST1 < PST2. Moreover, when comparing the two methods, the differences in their predicted absolute barrier heights fall within

the range of 5 kcal/mol (~0.22 eV). Also, both methods predict similar energy changes between the *cis* and *trans* minima of PSTs (ΔE, Table 2), and the discrepancies between the two methods fall within 1.7 kcal/mol (0.073 eV, Table 2). Consequently, this analysis confirms the suitability of hh-TDA-BHHLYP for the previously mentioned free-energy calculations.

Pathway 2: Isomerization through Intersystem Crossings between S_0 and T_1 States. The thermal isomerization of AB-derived photoswitches has been proposed to involve two intersystem crossings between the S_0 and T_1 states. The first
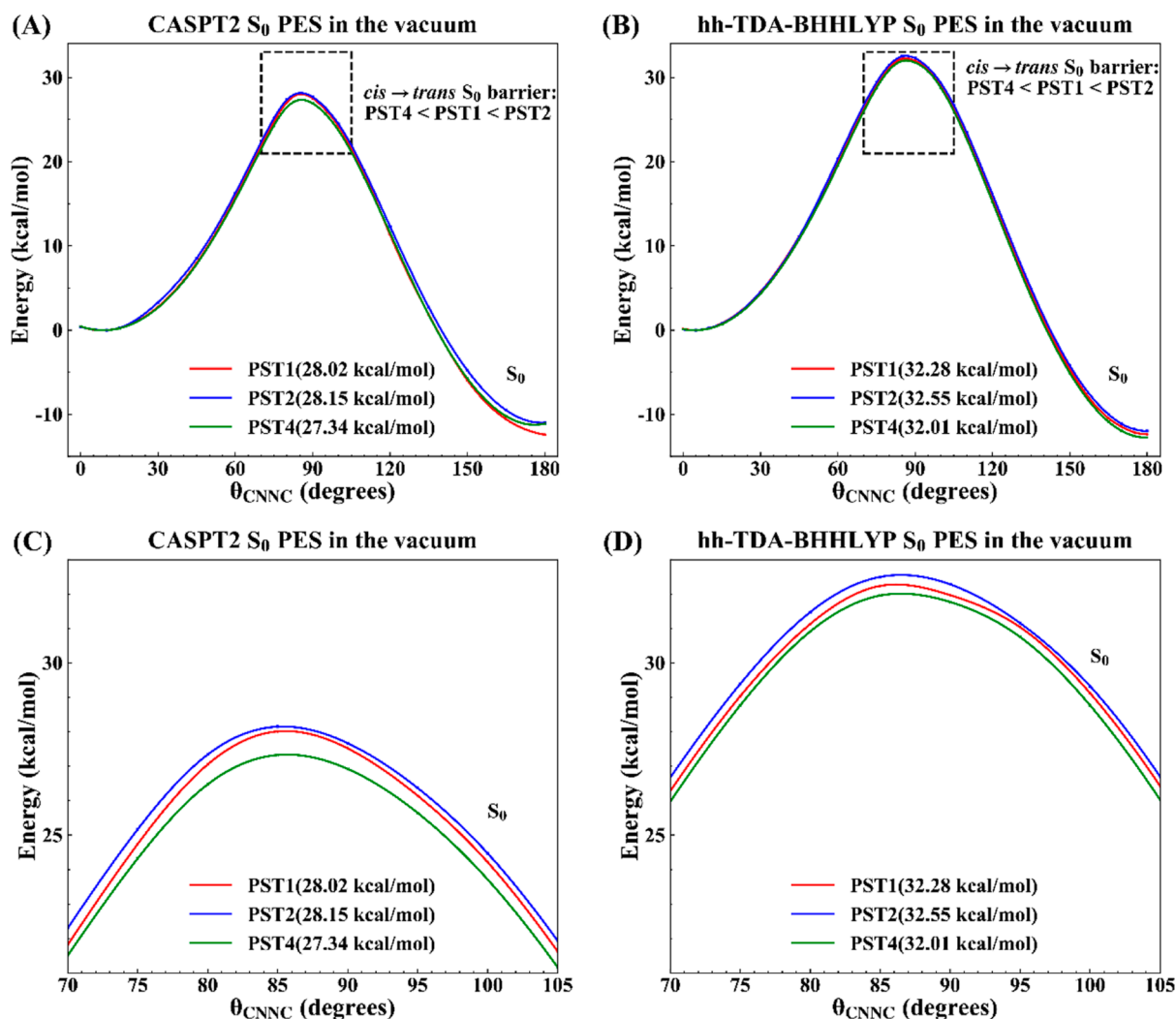
Figure 6. S_0 PES of PSTs along the central torsion θ_{CNNC} calculated by constrained optimization at (A) XMS-CASPT2 and (B) hh-TDA-BHHLYP levels of theory. The energy barriers from the *cis* minima to the barrier top are indicated in parentheses. The order of the barriers is indicated in the text. The PES curves near the barrier top (enclosed by the dashed black boxes) are zoomed out into (C,D) for better comparison between the PSTs. Both levels of theory predict the same relative order of the energy barriers among the three PSTs.

Table 2. Energy Difference (in kcal/mol) between the *cis* and *trans* Minima of PSTs on the S_0 State, Defined as $\Delta E = \Delta E_{cis} - \Delta E_{trans}$, Predicted by the XMS-CASPT2, Hh-TDA-BHHLYP, BHHLYP, and SF-TD-BHHLYP Methods[a]

	XMS-CASPT2	hh-TDA-BHHLYP	BHHLYP	SF-TD-BHHLYP
PST1	12.42	12.35	13.46	13.24
PST2	10.99	11.99	13.15	12.91
PST4	11.08	12.76	14.00	13.67

[a]All values are from PESs in a vacuum.

intersystem crossing occurs from the S_0 to T_1 state when the θ_{CNNC} torsion is between 70 and 90°, while the second takes place from T_1 to S_0 state within a 90−110° range. The $S_0 \rightarrow T_1 \rightarrow S_0$ pathway is considered more kinetically competitive than the S_0-only pathway due to the higher energy barrier of the latter. To investigate the probability of this alternative pathway, we performed constrained optimizations using both XMS-CASPT2 and hh-TDA-BHHLYP levels of theory on the S_0 and T_1 states and calculated the PESs of these states along the θ_{CNNC} torsion (Figure 7).

Both methods indicate that the $S_0 \rightarrow T_1 \rightarrow S_0$ pathway features lower barriers compared to the S_0-only pathway, while maintaining the same barrier order among the three PSTs, as

observed in the latter (Figure 6). Both methods predict that the higher intersystem crossing point occurs within a θ_{CNNC} torsion range of 75−85°. However, hh-TDA-BHHLYP overestimates the barrier height in this pathway by 6−7 kcal/mol compared to the XMS-CASPT2 method, due to the overestimation of the T_1 state's energy. Consequently, hh-TDA-BHHLYP predicts this pathway to be kinetically less likely than the XMS-CASPT2 prediction. Therefore, in the subsequent discussion, we present our analysis of the rates along this pathway using the more accurate XMS-CASPT2 method.

The *cis* → *trans* isomerization rates for the S_0-only and $S_0 \rightarrow T_1 \rightarrow S_0$ pathways were computed using the standard transition-state theory (k_{TST}, eq 1) and NA-TST ($k_{NA\text{-}TST}$, eq
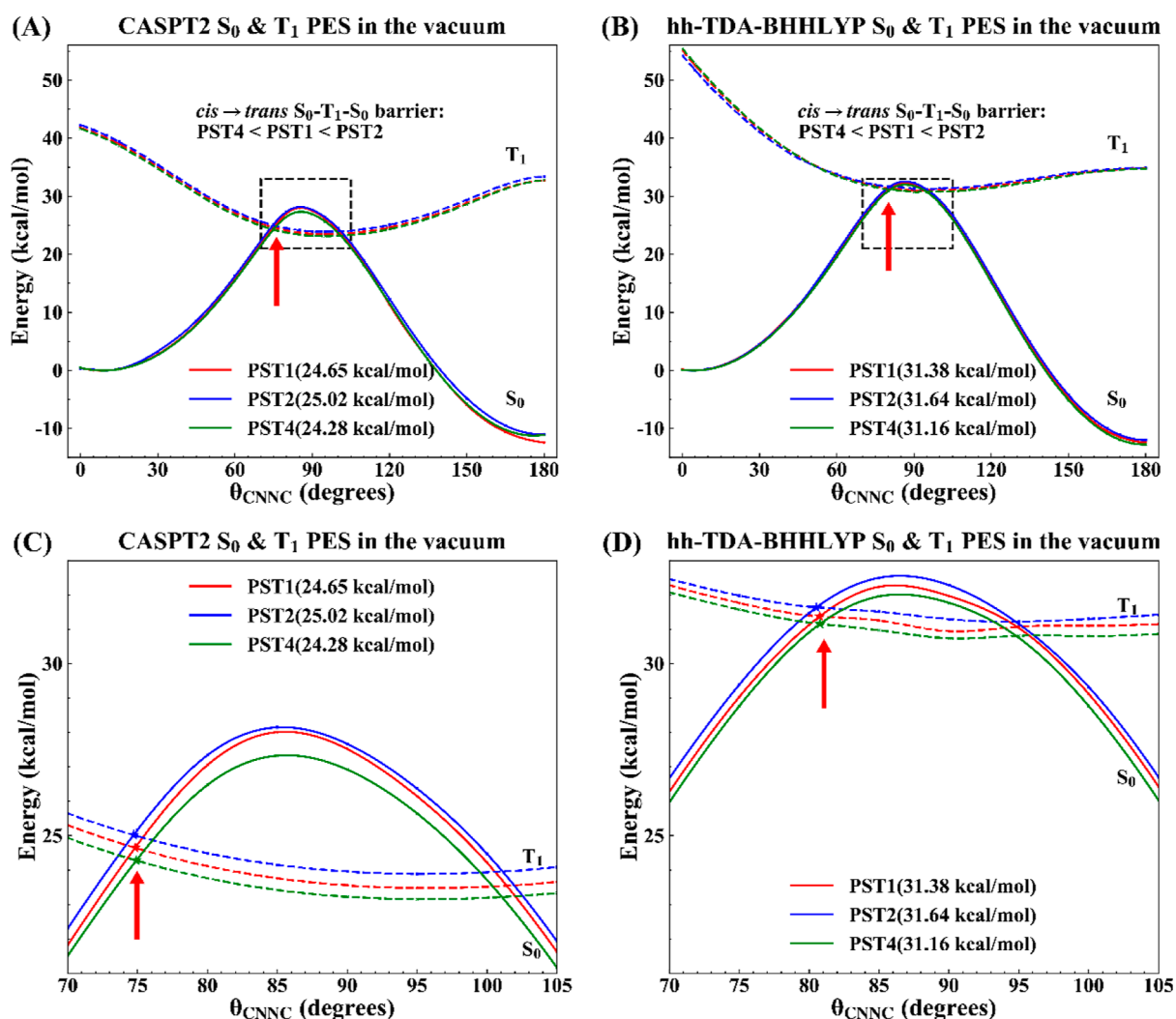
Figure 7. S_0 and T_1 PESs along the central torsion θ_{CNNC} calculated by constrained optimization at (A) XMS-CASPT2 and (B) hh-TDA-BHHLYP levels of theory. The energy gap between the S_0 *cis* minima and the higher of the two S_0-T_1 crossing points (indicated by red arrows) determines the energy barrier along the $S_0 \to T_1 \to S_0$ pathway, which is shown in the parentheses. The order of the barriers is indicated in the text. The PES curves near the S_0-T_1 crossing points (enclosed by the dashed black boxes) are zoomed out in (C,D) for a better comparison between the three PSTs. Both levels of theory predict the same relative order of the energy barriers among the three PSTs along the $S_0 \to T_1 \to S_0$ pathway. The order of barriers in this pathway is the same as that in the S_0-only pathway (Figure 3).

2 −9), respectively, with the results summarized in Table 3. The energy barriers used for rate calculations are summarized in Figures 6A and 7A. In the k_{NA-TST} calculations, SOCs (H_{SO}) between S_0 and T_1, as well as the gradients of both states at the highest intersystem crossing point, were determined to estimate the intersystem crossing rates (k_{ISC}). It becomes clear from Table 3 that the order of the three PSTs' k_{NA-TST} is consistent with the order of their energy barriers (Figure 7A).

Table 3. Thermal Isomerization Rates of PSTs in a Vacuum along the S_0-Only (k_{TST}) and $S_0 \to T_1 \to S_0$ (k_{NA-TST}) Pathways, Calculated at the XMS-CASPT2 Level of Theory[a]

|	k_{NA-TST} (s^{-1})	k_{ISC} (s^{-1})	H_{SO} (cm^{-1})	k_{TST} (s^{-1})
PST1	3.4399×10^{-8}	4.1156×10^{10}	19.015	1.7536×10^{-8}
PST2	1.6833×10^{-8}	3.7618×10^{10}	18.226	1.4079×10^{-8}
PST4	5.7921×10^{-8}	3.7100×10^{10}	17.988	5.5286×10^{-8}

[a]The SOC (H_{SO}) and intersystem crossing rates (k_{ISC}) used to calculate k_{NA-TST} are also summarized.

This is because H_{SO}'s are similar for all PSTs, resulting in comparable k_{ISC} values (Table 3), and thus the main factor influencing k_{NA-TST}'s in eq 3 is the energy barrier.

Comparing k_{NA-TST} and k_{TST}, it is evident that the $S_0 \to T_1 \to S_0$ pathway is not substantially faster than the S_0-only pathway, with their rate difference within *a* factor of 2. Importantly, the order of rates among the PSTs remains consistent across both pathways. Consequently, these findings support the use of only the S_0 state for free-energy calculations in a condensed phase environment when comparing the relative barrier heights among the PSTs and their kinetics in various environments.

Pathway 3: Isomerization through the Inversion of Bending Angles. Another isomerization mechanism frequently proposed for AB-based molecular photoswitches involves inversion through the bending angles near the N═N double bond (α_1 and α_2 in Figure 8A). The transition state of this inversion mechanism exhibits either α_1 or α_2 near 180°. To evaluate this hypothesis, we carried out a constrained optimization of PST1 along these two bending angles, ranging
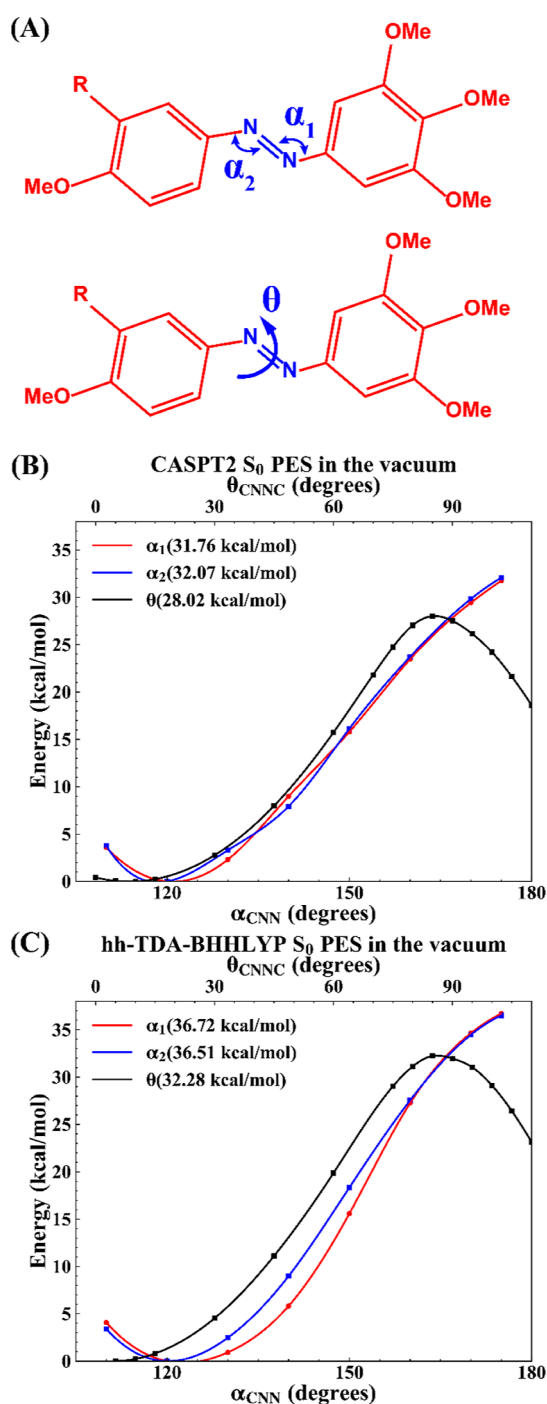
Figure 8. (A) Definition of the α_1 and α_2 bending angles in the PSTs. (B) and (C): PESs of PST1 along the two α_{CNN} bending angles calculated by constrained optimization at (XMS-)CASPT2 and hh-TDA-BHHLYP levels of theory, respectively. The PESs along the α_1 and α_2 angles (red and blue) are represented by the bottom x axis. As a comparison, the PESs along the central torsion θ_{CNNC} (black) are represented by the top x axis in each subplot. Both levels of theory predict that the rotation of θ_{CNNC} torsion has lower energy barriers than the inversion of the α_{CNN} angles.

from $\sim 120°$ near the *cis* minima to nearly $\sim 180°$ at the transition state. The PESs along the bending angles are compared with the PES along the central torsion θ in Figures 8B,C. Both methods predict that the angle inversion pathway has energy barriers at least 5 kcal/mol higher than those of the

torsion pathway, regardless of which angle is inverted. Thus, hh-TDA-BHHLYP accurately reproduces the XMS-CASPT2 result, which indicates that the inversion mechanism is kinetically less favorable than the torsion mechanism.

In contrast, when the PES scan was conducted along the central torsion using DFT with the BHHLYP functional (Figure 9A), the α_1 angle relaxes to $\sim 180°$ near the transition state (Figure 9B). A similar transition-state structure is observed using DFT with the ωPBEh functional (data not shown). The DFT's transition state structure starkly contrasts with those predicted using the hh-TDA-BHHLYP and XMS-CASPT2 methods (Figure 9B) near the S_0 state's barrier top (Figure 6A). Our results indicate that DFT erroneously favors the inversion mechanism over the torsional one, which is a major defect of this method. The failure of DFT to qualitatively predict the transition-state structure can be attributed to the single-reference method's inability to treat the multireference electronic structure near the transition state, where the energy gap between the S_0 and S_1 states is small (~ 0.8 eV, as predicted by XMS-CASPT2) due to the proximity to a conical intersection. Indeed, near the transition state, the CASSCF reference wavefunctions predict strong mixing of the $n\pi^*$ open-shell and ground-state closed-shell singlet electron configurations. Such multireference characters cannot be addressed by single-reference DFT methods by design.

In a previous study, Muždalo et al.[56] employed transition path sampling (TPS)[57] to extensively explore the isomerization pathway of AB and push−pull AB (pp-AB). The strength of TPS is that it does not assume predefined reaction coordinates and can provide rich dynamical information on the barrier-crossing events by analyzing the ensemble of trajectories connecting the reactant and product minima. The study[56] provided insights into how the isomerization mechanism changes in different solvent environments. Specifically, when transitioning from an implicit to explicit DMSO solvent environment, the isomerization mechanism shifts from inversion to rotation for pp-AB. Furthermore, their simulation indicated that in a vacuum environment, the inversion mechanism is likely to be the predominant pathway for pp-AB. However, it is worth noting that a semiempirical QM method (DFTB3) was employed in the QM/MM TPS simulations due to its optimal balance between efficiency and accuracy. Since the DFTB3 method is an approximation of DFT, it is a single-reference method with less accuracy than the ab initio multireference electronic structure methods such as XMS-CASPT2.

Our benchmark analysis uncovered DFT's artificial bias toward the inversion mechanism. Our results emphasize the importance of using the electronic structure methods that incorporate both static and dynamic electronic correlations, such as hh-TDA-DFT and XMS-CASPT2, to describe the reaction pathway across the TS correctly. Consequently, the conclusions drawn in the previous study[56] may have been biased by their selection of the semiempirical QM method, which does not accurately treat the electron correlation in the photoswitches.

In the Supporting Information (Table S5), we compare the experimental and calculated absolute thermal isomerization rates. The comparison reveals that both hh-TDA-DFT and XMS-CASPT2 levels of theory significantly underestimated the experimental rates. Currently, achieving a quantitative agreement between experiment and simulation in the absolute thermal isomerization kinetics remains a major challenge. This
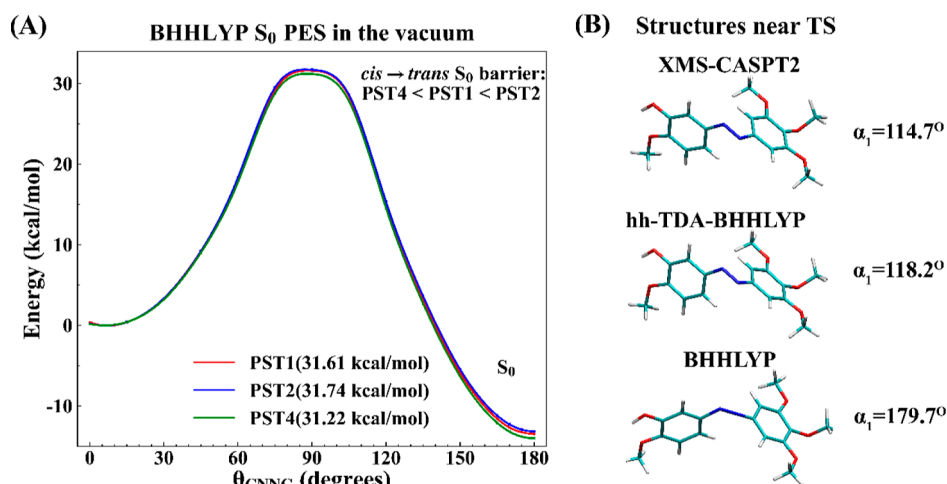
Figure 9. (A) S_0 PES of the three PSTs along the central torsion θ_{CNNC} calculated by constrained optimization using DFT with the BHHLYP functional. (B) Structures of PST1 near the S_0 PES barrier top predicted by XMS-CASPT2, hh-TDA-BHHLYP, and DFT(BHHLYP). Due to the lack of static correlation, DFT incorrectly predicts a transition state featuring a significant increase of the α_1 bending angle close to 180°, corresponding to the inversion mechanism. This structure is qualitatively different from the transition state predicted by the XMS-CASPT2 and hh-TDA-BHHLYP methods, which features ~90° θ_{CNNC} torsion without significant bending of the α_{CNN} angle, corresponding to the rotational mechanism.

challenge stems from the challenge to balance the accuracy and efficiency of correlated electronic structure methods. The section below provides a detailed analysis of the accuracy of the XMS-CASPT2 calculations and highlights the challenges for quantitatively predicting the experimental rate constants. Nonetheless, our hh-TDA-DFT/MM free-energy calculations in the aqueous solution accurately predict the relative order of experimental rates among the PSTs, which is essential for design purposes. The hh-TDA-DFT method has a decent balance between accuracy and efficiency for QM/MM free-energy simulations. Importantly, its capability to treat static correlation enables correct prediction of the rotational isomerization mechanism. As a result, we chose this method to gain a semiquantitative understanding of the isomerization mechanism in complex condensed-phase environments.

Validation of XMS-CASPT2 Calculations with the (10e,8o) Active Space. In the (10e,8o) active space for *cis* PST1 (Figure S2), all π and π^* orbitals are localized on the benzyl rings with the hydroxyl substituent, and there appears to be only one n orbital localized on one of the two central nitrogen atoms. At first glance, this choice of active space may seem to be unbalanced. However, we note that the n and π orbitals are mixed at the *cis* isomer minimum. The first two "π" orbitals (labeled in the upper two panels in Figure S2) have some character of n orbitals from the two central nitrogen atoms. Also, the substituents on the two benzyl rings are different: one benzyl ring carries one hydroxyl and one methoxy group, whereas the other benzyl ring carries three methoxy groups. Thus, we expect that the asymmetry of orbital localization in the (10e,8o) active space may arise from the mixing of the n and π orbitals and the inherently asymmetric electron distribution in the two benzyl rings. To justify our argument, we depicted the active space orbitals for the *trans* isomer of PST1 at $\theta_{CNNC} = 180°$ in Figure S3. This geometry was obtained using constrained optimization at the XMS-CASPT2/SA-3-CASSCF(10e,8o)/cc-pVDZ level of theory. It is evident that the (10e,8o) active space incorporates π and π^* orbitals in both benzyl rings, and the two n orbitals are symmetrically distributed between the two central nitrogen

atoms. From a technical point of view, it is noteworthy that our XMS-CASPT2 relaxed PES scans were performed by gradually and continuously twisting the *trans* isomer to the *cis* isomer with small intervals of θ_{CNNC} torsion. At each θ_{CNNC} value, the initial guess of CASSCF orbitals was obtained from the optimized CASSCF orbitals for the geometry with the adjacent θ_{CNNC} value. We observe that the active space orbitals gradually get localized to one of the two benzyl rings as the θ_{CNNC} torsion decreases from ° to 0°. Thus, the asymmetric distribution of the active space orbitals in Figure S2 arises as the *trans*-PST is gradually transformed into the *cis*-PST in our calculations.

To further validate our main conclusions from the XMS-CASPT2/SA-3-CASSCF(10e,8o)/cc-pVDZ calculations and justify the choice of active space orbitals, we performed single-point energy calculations using XMS-CASPT2 with a larger active space (14 electrons and 13 orbitals) and basis set (ANO-L-VDZP), i.e., XMS-CASPT2/SA-3-CASSCF-(14e,13o)/ANO-L-VDZP. The larger (14e,13o) active space contains π and π^* orbitals localized on both the benzyl rings of the *cis*-PSTs and the two central nitrogen atoms, as well as the n orbitals localized on the two nitrogen atoms. The orbitals of this larger active space are depicted in Figure S4. The geometries used for these single-point energy calculations were obtained from constrained optimizations at the XMS-CASPT2/SA-3-CASSCF(10e,8o) level of theory, with the θ_{CNNC} torsion fixed at 10 and 85°. These two torsion values were chosen because they are closest to the *cis* minima and barrier tops of the S_0-state PES calculated at the XMS-CASPT2/SA-3-CASSCF(10e,8o)/cc-pVDZ level of theory. For each type of PST, the *cis*-to-*trans* isomerization energy barrier along the S_0-only torsional pathway is estimated as the difference in the energies calculated at these two θ_{CNNC} values and summarized in Table S6. The two XMS-CASPT2 methods with (10e,8o) and (14e,13o) active spaces predict the same order of barriers across the three PSTs: PST4 < PST1 < PST2. Moreover, the XMS-CASPT2 calculations using the larger active space predict lower barriers for isomerization than the smaller active space. Thus, we conclude that using the (10e,8o)
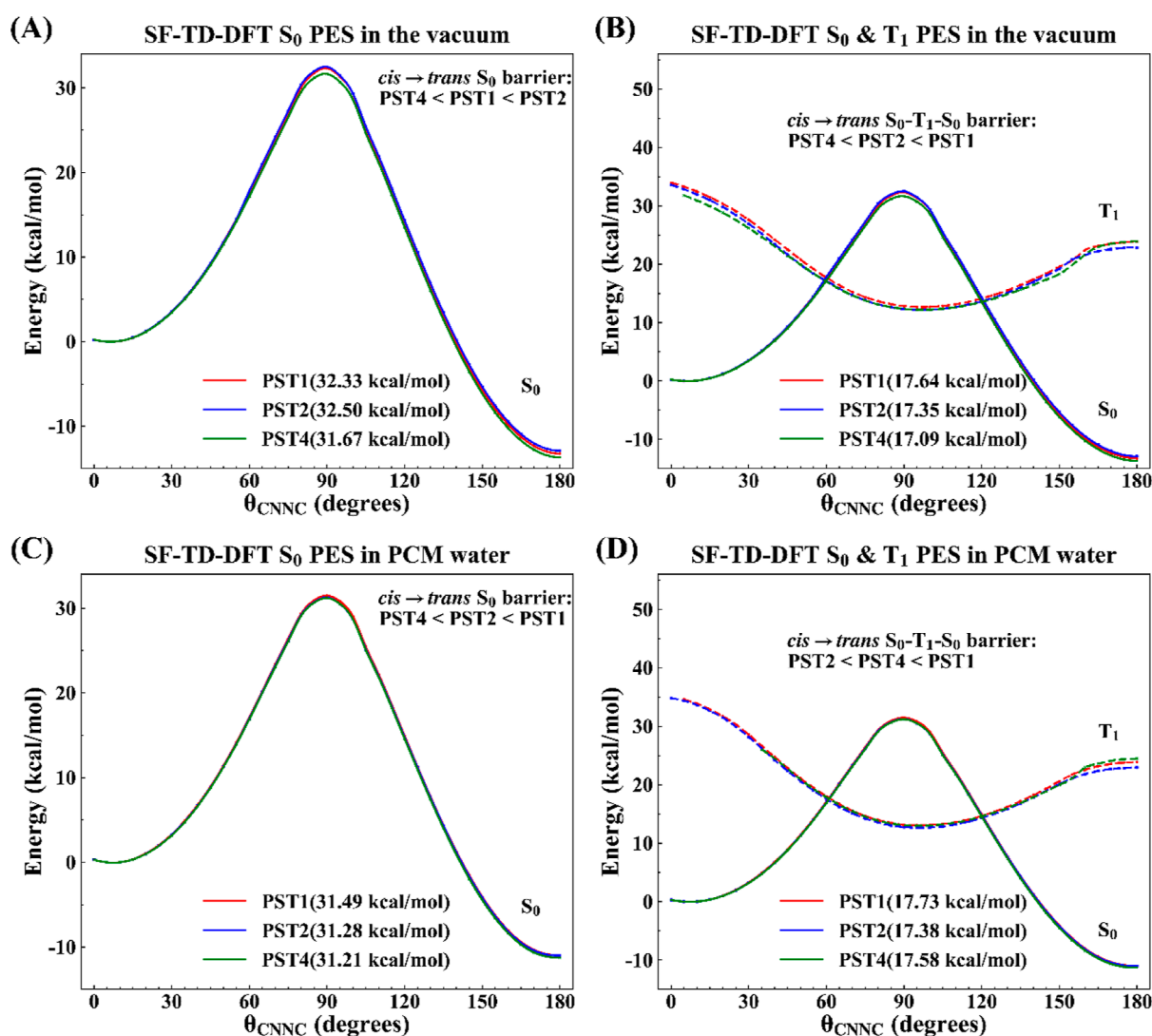
Figure 10. S_0 and T_1 PES of PSTs along the central torsion calculated by constrained optimization at SF-TD-DFT levels using the BHHLYP functional. (A) S_0 PES in a vacuum. (B) S_0 and T_1 PESs in a vacuum. (C) S_0 PES in implicit water. (D) S_0 and T_1 PESs in implicit water. In each subplot, energy barriers are indicated in parentheses, with their relative order labeled in the text. For isomerization pathway that only involves the S_0 state (A,C), the barriers are defined as the energy difference between the S_0 cis minima and the barrier top. For isomerization along the $S_0 \rightarrow T_1 \rightarrow S_0$ pathway, the barriers are defined as the energy difference between the S_0 cis minima and the higher of the two S_0-T_1 crossing points. The inclusion of implicit solvent perturbs the relative order of the barriers in a vacuum but cannot fully reproduce the experimental order of cis-PSTs' half-lives (Table 1).

active space is valid for predicting relative energy barriers but will overestimate the absolute barriers and thus underestimate the rate constants compared to the experiments, as shown in Table S5.

Our data suggest that using a larger active space and basis set can improve the agreement between the XMS-CASPT2 calculation and experiment. However, doing so will make the XMS-CASPT2 gradient calculations computationally too expensive to carry out relaxed PES scans along the reaction coordinates. Because relaxed PES scans are essential for accurately characterizing the reaction pathways, and the (10e,8o) active space correctly predicts the relative orders of barriers across the three PSTs, we adhere to this smaller but more cost-efficient active space for all our XMS-CASPT2 benchmark calculations.

Effects of Implicit Solvation on the Isomerization Barriers. To examine the effects of implicit solvation on the isomerization energy barriers, the PESs along the central torsion were calculated in both vacuum and implicit water at the SF-TD-DFT (BHHLYP functional) level of theory. Both the S_0-only and $S_0 \rightarrow T_1 \rightarrow S_0$ pathways were investigated for each PST. Similar to hh-TDA-DFT, SF-TD-DFT is a multireference method that accounts for static correlation near the isomerization transition state. Axelrod et al. recently employed this method to train machine learning models for quickly predicting thermal half-lives of AB derivatives in solution. In that study, both the $S_0 \rightarrow T_1 \rightarrow S_0$ pathway and implicit solvation effects were taken into account when constructing the training dataset.[9]

Comparing Figure 10A and C, the order of S_0-state barriers changes when transitioning from a vacuum to implicit water. The same observation can be made by comparing Figure 10B and D. However, even after incorporating implicit solvation, the order of barriers among the three PSTs still does not fully match that of the free-energy barriers in the explicit solvent (Figure 3B) or the experimental order of half-lives (Table 1).

Additionally, the SF-TD-DFT method overstabilizes the T_1 state compared to the XMS-CASPT2 calculations, resulting in barriers through the $S_0 \rightarrow T_1 \rightarrow S_0$ pathway that are ~7 kcal/mol lower than the benchmark calculations. Consequently, SF-TD-DFT significantly overestimates the likelihood of the $S_0 \rightarrow T_1 \rightarrow S_0$ pathway. We conclude that explicit solvation combined with the sampling of conformational fluctuations is necessary to fully reproduce the experimental order of PSTs' thermal half-lives.

Our results show that the SF-TD-DFT and hh-TDA-DFT methods predict similar S_0 barriers for the isomerization. Thus, the SF-TD-DFT method might also be a suitable choice, at least for the free-energy calculations on the S_0 state. However, we encountered a technical issue to use this method in our study. Our QM/MM US simulations were carried out using the TERACHEM software package, which significantly benefits from the GPU-accelerated electronic structure calculations that make such simulations cost-effective. Unfortunately, our current version of TERACHEM lacks the implementation of gradient calculations at the SF-TD-DFT level of theory. Thus, using SF-TD-DFT in TERACHEM, we can only run single-point energy calculations but not QM/MM US simulations. Although we employed the ORCA software package for constrained geometry optimizations during the PES scan (Figure 10), this package currently does not have an efficient GPU implementation, and the computational cost can be too prohibitive to run QM/MM US simulations on the CPUs. For these reasons, we only used hh-TDA-DFT to run QM/MM US simulations in explicit solvent and protein systems.

It is worth noting that an improved version of the conventional SF-TDDFT-TDA, namely the 'SF2' method, has been benchmarked in the past for investigating the photochemical cis−trans double-bond isomerization in a protonated Schiff-base model (PSB3) in a study by Xu et al.[58] The authors solved the excited-state spin-contamination problem of the original SF-TDDFT and can accurately describe the excited-state PES near the CI between the S_0 and S_1 states. However, the SF2 method treats the ground state with restricted closed-shell DFT, which cannot fully describe the static correlation near the transition state, as elucidated in our standard DFT calculations above (Figure 9). Thus, this method needs further development to accurately describe the ground-state isomerization of PSTs.

Isomerization through the Hydrazone Tautomer of Protonated PSTs. Previous studies have identified an alternative isomerization mechanism for AB-derived photoswitches, which involves the hydrazone tautomer of protonated AB as an intermediate (Figure 11A).[8,59−62] On one hand, protonation of one nitrogen atom in the N═N bond decreases the bond order, which generally lowers the isomerization barrier. On the other hand, due to the low pK_a's of the nitrogen atoms in the N═N double bonds (−2.95), protonation at these sites would be endergonic, which increases the overall barrier. Therefore, the balance between these two opposing effects determines whether the hydrazone tautomer pathway is kinetically more favorable than the unprotonated one.

The hydrazone tautomer can be stabilized by the electron-donating substituents on the benzyl ring at the para- and ortho-positions of the azo group (Figure 11A). Since methoxy groups are generally regarded as electron-donating in these positions, the pK_a's of the nitrogen atoms in PSTs could be higher than that in prototypical AB, potentially making the hydrazone tautomer mechanism more feasible. Consequently,
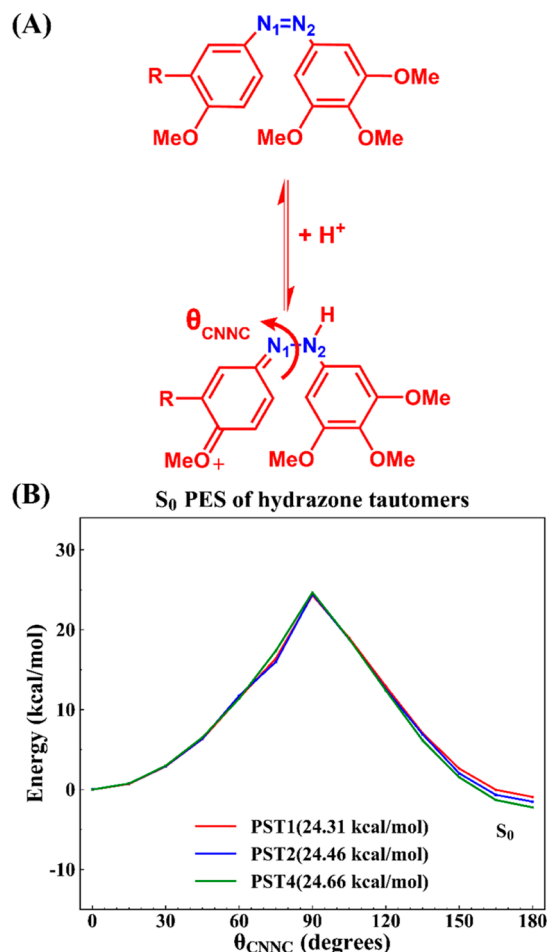
Figure 11. (A) Isomerization mechanism involving protonated PSTs in the hydrazone tautomer. (B) PES along the central torsion θ_{CNNC} of azo-hydrazone calculated by constrained optimization using hh-TDA-BHHLYP, with barriers indicated in the parentheses. Protonation on the N atom lowers the N═N bond order and reduces the isomerization barrier.

it is crucial to quantify the energy barriers associated with this pathway and compare them with the unprotonated pathway.

Prior computational studies have explored this isomerization mechanism using single-reference DFT methods[8] but without explicitly calculating the pK_a's for these compounds. To address this, we first carried out pK_a calculations for the nitrogen atoms in the three PSTs using the thermodynamic cycle (Figure 2) and eq 10.[46] (see "Methods"). The pK_a's of the N2 atom (labeled in Figure 11A) are summarized in Table 4, with their systematic errors corrected using the calculated and experimental pK_a's of trans-AZB.

The isomerization energy barrier of the hydrazone tautomer was determined using relaxed PES scans with the hh-TDA-BHHLYP method (Figure 11B). The total energy barrier for this pathway (Table 4) is estimated as the sum of the protonation free-energy barrier (eq 11) and the isomerization energy barrier. As shown in Table 4, the total energy barrier for this pathway is 1−2 kcal/mol higher than that of the unprotonated isomerization pathways involving only the S_0 state or the $S_0 \rightarrow T_1 \rightarrow S_0$ pathways. Furthermore, the corrected pK_a's are significantly lower than 7, suggesting that only a small population of the PSTs will be protonated in the hydrazone tautomer at room temperature and physiological

Table 4. Total _cis_ → _trans_ Energy Barrier ($\Delta E_1^{\ddagger}$) through the Hydrazone Intermediate at pH = 7[a]

	$\Delta E_1^{\ddagger b}$ (kcal/mol)	calculated pK_a	corrected[c] pK_a	$\Delta E_2^{\ddagger}$ (kcal/mol)	$\Delta E_3^{\ddagger}$ (kcal/mol)
PST1	32.90	7.78	0.71	32.28	31.38
PST2	33.88	7.17	0.10	32.55	31.64
PST4	33.71	7.44	0.37	32.01	31.16
trans-AZB	N/A	4.12	−2.95	N/A	N/A

[a]The isomerization energy barriers for the unprotonated PST isomerization along the S_0-only pathway ($\Delta E_2^{\ddagger}$, from Figure 6B) and $S_0 \rightarrow T_1 \rightarrow S_0$ pathways ($\Delta E_3^{\ddagger}$, from Figure 7B) are compared with $\Delta E_1^{\ddagger}$. The isomerization through the hydrazone intermediate is not as kinetically favorable as that through the unprotonated PST. [b]$\Delta E_1^{\ddagger}$ is calculated by summing the free-energy change of protonating PST at N2 at pH = 7 and the rotational barrier of the hydrazone tautomer listed in Figure 11B. [c]The calculated pK_a's of PSTs are corrected based on the calculated and experimental pK_a's of _trans_-AB (_trans_-AZB) listed in the last row. Corrected pK_a's are used for calculating $\Delta E_1^{\ddagger}$.

pH conditions according to the Boltzmann distribution. However, all the three PSTs have higher pK_a's than _trans_-AZB by ∼3 pH units (Table 4), which confirms that the methoxy substituents stabilize the hydrazone tautomer. Overall, the hydrazone mechanism is less kinetically favorable than the unprotonated PST mechanism. The protein environment or the introduction of different substituents on the benzyl ring may alter the pK_a's of the PSTs, making this alternative mechanism more competitive.

CONCLUSIONS

PSTs can reversibly inhibit MT polymerization with light control, making them potential cancer chemotherapeutics with minimal side effects. Using advanced QM/MM calculations and enhanced sampling, we examined the free-energy profiles of PSTs in various molecular environments. The calculations show that protein binding significantly impacts the thermal isomerization barriers of _cis_-PSTs due to complex protein–ligand interactions. Additionally, our free-energy calculations in explicit water align with the experimental order of PSTs' thermal half-lives, suggesting that solvation can alter the order of isomerization free-energy barriers.

Our benchmark calculations confirm the accuracy of hh-TDA-DFT for free-energy calculations. This method reproduces the order of isomerization barriers of three PSTs predicted by the XMS-CASPT2 method in a vacuum along both S_0-only and $S_0 \rightarrow T_1 \rightarrow S_0$ pathways. By including static correlation, hh-TDA-DFT overcomes DFT's limitations and accurately predicts the torsional mechanism to be more favorable than the bending angle inversion mechanism. Employing NA-TST and XMS-CASPT2 calculations, we find that the $S_0 \rightarrow T_1 \rightarrow S_0$ pathway is modestly faster than the S_0-only pathway, and the two pathways share the same order of kinetics among the three PSTs, justifying the free-energy calculations on the S_0 state. Our SF-TD-DFT calculations reveal that implicit solvation models cannot fully reproduce the experimental order of barriers. Thus, conformational sampling in explicit solvents with multireference electronic structure methods is required to accurately reproduce experimental thermal half-lives.

Moreover, we investigated isomerization through protonated PSTs in the hydrazone tautomer using pK_a calculations and torsional PES analysis. The results show that PSTs have higher pK_a's than _trans_-AZB due to the electron-donating groups on the benzyl rings, and the isomerization barrier of the hydrazone is lower than that of unprotonated PSTs. However, the hydrazone tautomer pathway's total energy barriers are slightly higher than the unprotonated pathway, and the latter is thus kinetically more favorable. Stronger electron-donating substituents on the benzyl ring could make the hydrazone

tautomer pathway more feasible. Overall, our work offers valuable insights into the thermal isomerization mechanism of photoswitches in biological environments. Also, to the best of our knowledge, this is the first time that a comprehensive characterization of all competing isomerization pathways is performed using accurate ab initio multireference electronic structure methods (hh-TDA-DFT and XMS-CASPT2). From a methodological point of view, our work establishes comprehensive and high-quality benchmark data that will guide the choice of different computational methods to study the thermal isomerization of molecular photoswitches. Importantly, multireference methods and explicit molecular environment treatment are necessary to accurately predict the experimental data.

ASSOCIATED CONTENT

Supporting Information

The Supporting Information is available free of charge at https://pubs.acs.org/doi/10.1021/acs.jctc.3c00451.

Comparison between crystal structure and equilibrated structure, active space orbitals, structures of the _cis_ minima, MECP and TS of the three PSTs, RDFs between the PST and water molecules in the aqueous solution. Relative energies of the _cis_ minima, MECP and TS; frequencies to observe water-mediated intramolecular hydrogen bonds; comparison of experimental and calculated isomerization rate constants; and XMS-CASPT2 single-point energies at the _cis_ minima and S_0-state barrier top with the (14e,13o) active space (PDF)

AUTHOR INFORMATION

Corresponding Author

Ruibin Liang − _Department of Chemistry and Biochemistry, Texas Tech University, Lubbock, Texas 79409, United States;_ orcid.org/0000-0001-8741-1520; Email: rliang@ttu.edu

Authors

Amirhossein Bakhtiiari − _Department of Chemistry and Biochemistry, Texas Tech University, Lubbock, Texas 79409, United States_

Gustavo J. Costa − _Department of Chemistry and Biochemistry, Texas Tech University, Lubbock, Texas 79409, United States_

Complete contact information is available at:
https://pubs.acs.org/10.1021/acs.jctc.3c00451

Notes

The authors declare no competing financial interest.

■ REFERENCES

(1) Hüll, K.; Morstein, J.; Trauner, D. In Vivo Photopharmacology. *Chem. Rev.* **2018**, *118*, 10710−10747.

(2) Szymański, W.; Beierle, J. M.; Kistemaker, H. A. V.; Velema, W. A.; Feringa, B. L. Reversible Photocontrol of Biological Systems by the Incorporation of Molecular Photoswitches. *Chem. Rev.* **2013**, *113*, 6114−6178.

(3) Mukhopadhyay, T. K.; Morstein, J.; Trauner, D. Photopharmacological control of cell signaling with photoswitchable lipids. *Curr. Opin. Pharmacol.* **2022**, *63*, 102202.

(4) Tochitsky, I.; Kienzler, M. A.; Isacoff, E.; Kramer, R. H. Restoring Vision to the Blind with Chemical Photoswitches. *Chem. Rev.* **2018**, *118*, 10748−10773.

(5) Dokić, J.; Gothe, M.; Wirth, J.; Peters, M. V.; Schwarz, J.; Hecht, S.; Saalfrank, P. Quantum Chemical Investigation of Thermal Cis-to-Trans Isomerization of Azobenzene Derivatives: Substituent Effects, Solvent Effects, and Comparison to Experimental Data. *J. Phys. Chem. A* **2009**, *113*, 6763−6773.

(6) Mukadum, F.; Nguyen, Q.; Adrion, D. M.; Appleby, G.; Chen, R.; Dang, H.; Chang, R.; Garnett, R.; Lopez, S. A. Efficient Discovery of Visible Light-Activated Azoarene Photoswitches with Long Half-Lives Using Active Search. *J. Chem. Inf. Model.* **2021**, *61*, 5524−5534.

(7) Crecca, C. R.; Roitberg, A. E. Theoretical Study of the Isomerization Mechanism of Azobenzene and Disubstituted Azobenzene Derivatives. *J. Phys. Chem. A* **2006**, *110*, 8188−8203.

(8) Rickhoff, J.; Arndt, N. B.; Böckmann, M.; Doltsinis, N. L.; Ravoo, B. J.; Kortekaas, L. Reversible, Red-Shifted Photoisomerization in Protonated Azobenzenes. *J. Org. Chem.* **2022**, *87*, 10605−10612.

(9) Axelrod, S.; Shakhnovich, E.; Gómez-Bombarelli, R. Thermal Half-Lives of Azobenzene Derivatives: Virtual Screening Based on Intersystem Crossing Using a Machine Learning Potential. *ACS Cent. Sci.* **2023**, *9*, 166−176.

(10) Cembran, A.; Bernardi, F.; Garavelli, M.; Gagliardi, L.; Orlandi, G. On the Mechanism of the *cis−trans* Isomerization in the Lowest Electronic States of Azobenzene: S0, S1, and T1. *J. Am. Chem. Soc.* **2004**, *126*, 3234−3243.

(11) Gaspari, R.; Prota, A. E.; Bargsten, K.; Cavalli, A.; Steinmetz, M. O. Structural Basis of *cis*- and *trans*-Combretastatin Binding to Tubulin. *Chem* **2017**, *2*, 102−113.

(12) Borowiak, M.; Nahaboo, W.; Reynders, M.; Nekolla, K.; Jalinot, P.; Hasserodt, J.; Rehberg, M.; Delattre, M.; Zahler, S.; Vollmar, A.; et al. Photoswitchable Inhibitors of Microtubule Dynamics Optically Control Mitosis and Cell Death. *Cell* **2015**, *162*, 403−411.

(13) Dumontet, C.; Jordan, M. A. Microtubule-binding agents: a dynamic field of cancer therapeutics. *Nat. Rev. Drug Discovery* **2010**, *9*, 790−803.

(14) Jordan, A.; Hadfield, J. A.; Lawrence, N. J.; McGown, A. T. Tubulin as a target for anticancer drugs: Agents which interact with the mitotic spindle. *Med. Res. Rev.* **1998**, *18*, 259−296.

(15) Hooper, A. T.; Loganzo, F.; May, C.; Gerber, H.-P. Identification and Development of Vascular Disrupting Agents: Natural Products That Interfere with Tumor Growth. In *Natural Products and Cancer Drug Discovery*; Koehn, F. E., Ed.; Springer New York, 2013; pp 17−38.

(16) Stanton, R. A.; Gernert, K. M.; Nettles, J. H.; Aneja, R. Drugs that target dynamic microtubules: A new molecular perspective. *Med. Res. Rev.* **2011**, *31*, 443−481.

(17) Bannwarth, C.; Yu, J. K.; Hohenstein, E. G.; Martínez, T. J. Hole−hole Tamm−Dancoff-approximated density functional theory: A highly efficient electronic structure method incorporating dynamic and static correlation. *J. Chem. Phys.* **2020**, *153*, 024110.

(18) Yu, J. K.; Bannwarth, C.; Hohenstein, E. G.; Martínez, T. J. Ab Initio Nonadiabatic Molecular Dynamics with Hole−Hole Tamm−Dancoff Approximated Density Functional Theory. *J. Chem. Theory Comput.* **2020**, *16*, 5499−5511.

(19) Yu, J. K.; Bannwarth, C.; Liang, R.; Hohenstein, E. G.; Martínez, T. J. Nonadiabatic Dynamics Simulation of the Wavelength-Dependent Photochemistry of Azobenzene Excited to the nπ* and ππ* Excited States. *J. Am. Chem. Soc.* **2020**, *142*, 20680−20690.

(20) Liang, R. First-Principles Nonadiabatic Dynamics Simulation of Azobenzene Photodynamics in Solutions. *J. Chem. Theory Comput.* **2021**, *17*, 3019−3030.

(21) Liang, R.; Bakhtiiari, A. Multiscale simulation unravels the light-regulated reversible inhibition of dihydrofolate reductase by phototrexate. *J. Chem. Phys.* **2022**, *156*, 245102.

(22) Liang, R.; Bakhtiiari, A. Effects of Enzyme−Ligand Interactions on the Photoisomerization of a Light-Regulated Chemotherapeutic Drug. *J. Phys. Chem. B* **2022**, *126*, 2382−2393.

(23) Liang, R.; Das, D.; Bakhtiiari, A. Protein confinement fine-tunes aggregation-induced emission in human serum albumin. *Phys. Chem. Chem. Phys.* **2021**, *23*, 26263−26272.

(24) Shiozaki, T.; Győrffy, W.; Celani, P.; Werner, H.-J. Communication: Extended multi-state complete active space second-order perturbation theory: Energy and nuclear gradients. *J. Chem. Phys.* **2011**, *135*, 081106.

(25) Finley, J.; Malmqvist, P.-Å.; Roos, B. O.; Serrano-Andrés, L. The multi-state CASPT2 method. *Chem. Phys. Lett.* **1998**, *288*, 299−306.

(26) Andersson, K.; Malmqvist, P. Å.; Roos, B. O. Second-order perturbation theory with a complete active space self-consistent field reference function. *J. Chem. Phys.* **1992**, *96*, 1218−1226.

(27) Andersson, K.; Malmqvist, P. A.; Roos, B. O.; Sadlej, A. J.; Wolinski, K. Second-order perturbation theory with a CASSCF reference function. *J. Phys. Chem.* **1990**, *94*, 5483−5488.

(28) Webb, B.; Sali, A. Comparative Protein Structure Modeling Using MODELLER. *Curr. Protoc. Bioinf.* **2016**, *54*, 5.6.1−5.6.37.

(29) Gordon, J. C.; Myers, J. B.; Folta, T.; Shoja, V.; Heath, L. S.; Onufriev, A. H++: a server for estimating p Ka s and adding missing hydrogens to macromolecules. *Nucleic Acids Res.* **2005**, *33*, W368−W371.

(30) University of California. *Amber 2021*; University of California: San Francisco, 2021.

(31) Wang, J.; Wolf, R. M.; Caldwell, J. W.; Kollman, P. A.; Case, D. A. Development and testing of a general amber force field. *J. Comput. Chem.* **2004**, *25*, 1157−1174.

(32) Wang, J.; Wang, W.; Kollman, P. A.; Case, D. A. Automatic atom type and bond type perception in molecular mechanical calculations. *J. Mol. Graph. Model.* **2006**, *25*, 247−260.

(33) Meagher, K. L.; Redman, L. T.; Carlson, H. A. Development of polyphosphate parameters for use with the AMBER force field. *J. Comput. Chem.* **2003**, *24*, 1016−1025.

(34) Maier, J. A.; Martinez, C.; Kasavajhala, K.; Wickstrom, L.; Hauser, K. E.; Simmerling, C. ff14SB: Improving the Accuracy of Protein Side Chain and Backbone Parameters from ff99SB. *J. Chem. Theory Comput.* **2015**, *11*, 3696−3713.

(35) Dickson, C. J.; Madej, B. D.; Skjevik, Å. A.; Betz, R. M.; Teigen, K.; Gould, I. R.; Walker, R. C. Lipid14: The Amber Lipid Force Field. *J. Chem. Theory Comput.* **2014**, *10*, 865−879.

(36) Wu, Y. J.; Tepper, H. L.; Voth, G. A. Flexible simple point-charge water model with improved liquid-state properties. *J. Chem. Phys.* **2006**, *124*, 024503.

(37) Kumar, S.; Rosenberg, J. M.; Bouzida, D.; Swendsen, R. H.; Kollman, P. A. THE weighted histogram analysis method for free-energy calculations on biomolecules. I. The method. *J. Comput. Chem.* **1992**, *13*, 1011−1021.

(38) WHAM: the weighted histogram analysis method. http://membrane.urmc.rochester.edu/wordpress/?page_id=126 (accessed Jan 09, 2022).

(39) Malmqvist, P. Å.; Roos, B. O.; Schimmelpfennig, B. The restricted active space (RAS) state interaction approach with spin−orbit coupling. *Chem. Phys. Lett.* **2002**, *357*, 230−240.

(40) Roos, B. O.; Malmqvist, P.-Å. On the Effects of Spin−Orbit Coupling on Molecular Properties: Dipole Moment and Polarizability of PbO and Spectroscopic Constants for the Ground and Excited States. *Advances in Quantum Chemistry*; Academic Press, 2004; Vol. *47*, pp 37−49.

(41) Lykhin, A. O.; Kaliakin, D. S.; dePolo, G. E.; Kuzubov, A. A.; Varganov, S. A. Nonadiabatic transition state theory: Application to intersystem crossings in the active sites of metal-sulfur proteins. *Int. J. Quantum Chem.* **2016**, *116*, 750−761.

(42) Liu, S.; Srinivasan, S.; Tao, J.; Grady, M. C.; Soroush, M.; Rappe, A. M. Modeling Spin-Forbidden Monomer Self-Initiation Reactions in Spontaneous Free-Radical Polymerization of Acrylates and Methacrylates. *J. Phys. Chem. A* **2014**, *118*, 9310−9318.

(43) Liu, F.; Luehr, N.; Kulik, H. J.; Martínez, T. J. Quantum Chemistry for Solvated Molecules on Graphical Processing Units Using Polarizable Continuum Models. *J. Chem. Theory Comput.* **2015**, *11*, 3131−3144.

(44) Barone, V.; Cossi, M. Quantum Calculation of Molecular Energies and Energy Gradients in Solution by a Conductor Solvent Model. *J. Phys. Chem. A* **1998**, *102*, 1995−2001.

(45) Shao, Y.; Head-Gordon, M.; Krylov, A. I. The spin−flip approach within time-dependent density functional theory: Theory and applications to diradicals. *J. Chem. Phys.* **2003**, *118*, 4807−4818.

(46) Trummal, A.; Rummel, A.; Lippmaa, E.; Burk, P.; Koppel, I. A. IEF-PCM Calculations of Absolute pKa for Substituted Phenols in Dimethyl Sulfoxide and Acetonitrile Solutions. *J. Phys. Chem. A* **2009**, *113*, 6206−6212.

(47) Alongi, K. S.; Shields, G. C. Theoretical Calculations of Acid Dissociation Constants: A Review Article. In *Annual Reports in Computational Chemistry*; Wheeler, R. A., Ed.; Elsevier, 2010; Vol. *6*, Chapter 8, pp 113−138.

(48) Shiozaki, T. BAGEL: Brilliantly Advanced General Electronic-structure Library. *WIREs Comput. Mol. Biosci.* **2018**, *8*, No. e1331.

(49) BAGEL. *Brilliantly Advanced General Electronic-Structure Library*, http://www.nubakery.org (accessed Jan 09, 2020).

(50) Wang, L.-P.; Song, C. Geometry optimization made simple with translation and rotation coordinates. *J. Chem. Phys.* **2016**, *144*, 214108.

(51) FdezGalván, I.; Vacher, M.; Alavi, A.; Angeli, C.; Aquilante, F.; Autschbach, J.; Bao, J. J.; Bokarev, S. I.; Bogdanov, N. A.; Carlson, R. K.; et al. OpenMolcas: From Source Code to Insight. *J. Chem. Theory Comput.* **2019**, *15*, 5925−5964.

(52) Neese, F.; Wennmohs, F.; Becker, U.; Riplinger, C. The ORCA quantum chemistry program package. *J. Chem. Phys.* **2020**, *152*, 224108.

(53) Bonomi, M.; Branduardi, D.; Bussi, G.; Camilloni, C.; Provasi, D.; Raiteri, P.; Donadio, D.; Marinelli, F.; Pietrucci, F.; Broglia, R. A.; et al. PLUMED: A portable plugin for free-energy calculations with molecular dynamics. *Comput. Phys. Commun.* **2009**, *180*, 1961−1972.

(54) Tribello, G. A.; Bonomi, M.; Branduardi, D.; Camilloni, C.; Bussi, G. PLUMED 2: New feathers for an old bird. *Comput. Phys. Commun.* **2014**, *185*, 604−613.

(55) Bussi, G.; Camilloni, C.; Tribello, G. A.; Banáš, P.; Barducci, A.; Bernetti, M.; Bolhuis, P. G.; Bottaro, S.; Branduardi, D.; The PLUMED consortium; et al. Promoting transparency and reproducibility in enhanced molecular simulations. *Nat. Methods* **2019**, *16*, 670−673.

(56) Muždalo, A.; Saalfrank, P.; Vreede, J.; Santer, M. Cis-to-Trans Isomerization of Azobenzene Derivatives Studied with Transition Path Sampling and Quantum Mechanical/Molecular Mechanical Molecular Dynamics. *J. Chem. Theory Comput.* **2018**, *14*, 2042−2051.

(57) Bolhuis, P. G.; Chandler, D.; Dellago, C.; Geissler, P. L. Transition path sampling: Throwing ropes over rough mountain passes, in the dark. *Annu. Rev. Phys. Chem.* **2002**, *53*, 291−318.

(58) Xu, X.; Gozem, S.; Olivucci, M.; Truhlar, D. G. Combined Self-Consistent-Field and Spin-Flip Tamm−Dancoff Density Functional Approach to Potential Energy Surfaces for Photochemistry. *J. Phys. Chem. Lett.* **2013**, *4*, 253−258.

(59) Kojima, M.; Nebashi, S.; Ogawa, K.; Kurita, N. Effect of solvent on *cis*-to-*trans* isomerization of 4-hydroxyazobenzene aggregated through intermolecular hydrogen bonds. *J. Phys. Org. Chem.* **2005**, *18*, 994−1000.

(60) Matazo, D. R. C.; Ando, R. A.; Borin, A. C.; Santos, P. S. Azo−Hydrazone Tautomerism in Protonated Aminoazobenzenes: Resonance Raman Spectroscopy and Quantum-Chemical Calculations. *J. Phys. Chem. A* **2008**, *112*, 4437−4443.

(61) Garcia-Amorós, J.; Díaz-Lobo, M.; Nonell, S.; Velasco, D. Fastest Thermal Isomerization of an Azobenzene for Nanosecond Photoswitching Applications under Physiological Conditions. *Angew. Chem., Int. Ed.* **2012**, *51*, 12820−12823.

(62) Garcia-Amorós, J.; Sánchez-Ferrer, A.; Massad, W. A.; Nonell, S.; Velasco, D. Kinetic study of the fast thermal *cis*-to-*trans* isomerisation of para-ortho- and polyhydroxyazobenzenes. *Phys. Chem. Chem. Phys.* **2010**, *12*, 13238−13242.